

The detection efficiency of low-dose cryo-4D STEM for biogenic crystals in frozen-hydrated samples

Lothar Houben, *^a Zohar Eyal  and Dvir Gur  ^b

Received 31st January 2025, Accepted 7th April 2025

DOI: 10.1039/d5fd00027k

Multimodal scanning transmission electron microscopy on vitrified frozen-hydrated specimens promises exceptional spatial resolution into the molecular mechanisms underlying the formation of organic crystals in both health and disease. Detection of crystalline volumes is essential for tracking and mapping nucleation and growth. We provide an analytical description of the low-dose detection limit in diffraction for a thin crystal embedded in a thick matrix, focusing on organic crystals and embedding matrices of low-Z elements such as vitrified ice. Numerical calculations refine our description by accounting for the effects of multiple scattering. Often underestimated, wide-angle tails associated with inelastic scattering play a crucial role for the detection of crystalline reflections in a thick ice matrix, common for cryo-electron microscopy. We show that guanine crystals as thin as a few nanometers can be detected with a fluence of just a few thousand electrons if the ice thickness is below one mean free path for inelastic scattering. The required fluence increases non-linearly with the embedding ice thickness, with a pronounced top-bottom effect regarding the location of the crystal in the sample. Energy-filtered recording significantly reduces the fluence needed for thicker samples. The low-dose simulations implemented here validate the analytical description while acknowledging its limitations due to abstraction from multiple scattering and beam spreading.

Introduction

Biocrystallization and biominerization, influenced by biological environments, play crucial roles in life, from mechanical support,^{1–4} to light manipulation,^{5–7} to storage.^{8–11} These processes allow organisms to precisely control crystal formation, tailoring material properties to specific functional needs. By controlling nucleation and growth, organisms direct the formation of distinct polymorphs, morphologies, and spatial distributions, achieving remarkable structural

^aDepartment of Chemical Research Support, Weizmann Institute of Science, Rehovot, 7610001, Israel. E-mail: lothar.houben@weizmann.ac.il

^bDepartment of Molecular Genetics, Weizmann Institute of Science, Rehovot, 7610001, Israel



precision.^{3,4,12} Understanding the intricate molecular mechanisms and design strategies utilized by biological systems can inspire innovative biomimetic and bioenabled methods for producing functional materials under mild reaction conditions that avoid extreme temperatures and pressures or harsh chemicals, thus enhancing both safety and sustainability or biocompatibility. Part of this complexity arises from how organisms manipulate their local environments and compositions to create a diverse array of crystalline aggregates, both morphologically and functionally, through variations in local chemistry and different shaping techniques. The challenges posed by these processes under mild reaction conditions necessitate a multidisciplinary approach, utilizing experimental tools from biochemistry, molecular genetics, and molecular cell biology, alongside advanced spectrometry and microscopy methods.

Transmission electron microscopy (TEM) under cryogenic conditions has significantly enhanced our capacity to decipher biological matter within the context of its native cellular environment.¹³ Scanning transmission electron microscopy (STEM) offers distinct advantages over conventional wide-field TEM, particularly in terms of dose efficiency and tolerance for thicker specimens.^{14,15} Spatial information in STEM originates from the optical focusing of the electron probe. The diameter of the probe function and the scattering in the sample define the interaction volume, which can range from an Angstrom to tens of nanometers. STEM accommodates a wide range of post-specimen detectors, which allows for the analysis of a significant fraction of scattered electrons.¹⁶ These capabilities are fully leveraged in materials sciences,^{17–19} and analytical STEM equipped with energy dispersive X-ray spectroscopy (EDS), recording element-characteristic X-rays emitted from the sample upon electron irradiation, has provided valuable insights into the elemental distribution within entire freeze-dried cells.²⁰ In recent years, STEM has demonstrated the ability to image highly electron-beam-sensitive materials with segmented detectors.²¹

An exciting recent development is four-dimensional STEM (4D STEM). In 4D STEM, in each position of the rastering electron probe, a full diffraction pattern is recorded on a fast detection camera.²² The wealth of information in real space and diffraction space can be utilized for either phase identification, orientation determination, or chemical information. Novel 4D-STEM phase imaging techniques, such as differential phase contrast, ptychography, parallax imaging or tilt-corrected bright-field STEM, have recently shown their potential for low-dose imaging of vitrified frozen-hydrated biological specimens.^{23–25}

The application of 4D STEM to crystallization offers unparalleled sensitivity for detecting nanometric crystalline volumes and their respective phases, all while maintaining spatial resolution. The minimum mass detection for crystalline volumes is boosted compared to imaging techniques by the separation of unscattered electrons from scattered. The increase of the signal-to-background ratio is by the concentration of scattering in Bragg spots, common also to any dark-field detection in TEM, but in 4D STEM it occurs without apertures or segmented detection that would mean loss of dose efficiency.

Fig. 1 illustrates an instance where we utilized multimodal STEM characterization with 4D STEM acquisition to investigate the microenvironmental conditions that facilitate guanine accumulation and crystallization within zebrafish iridosomes.²⁶ Iridophores are specialized pigment cells that house reflective guanine crystals, which play a vital role in the vibrant and dynamic coloration



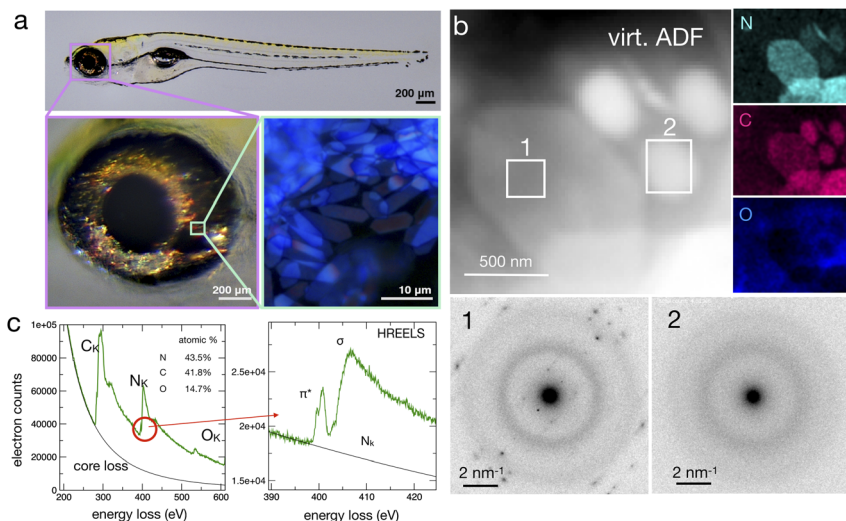


Fig. 1 Multimodal STEM characterisation of intracellular electron-dense vesicles abundant in zebrafish-larva iridophores.²⁶ (a) Incident light images of a zebrafish larva containing guanine crystals in its eyes and skin. Insets show higher magnifications of the eye and the crystals within it. (b) 4D STEM nanobeam diffraction and EDS data of guanine crystals and electron-dense intracellular organelles from isolated iridophores. Left: virtual annular dark-field image showing for each pixel the sum intensities of electrons that were scattered out of the electron incident beam direction. Right column: background-subtracted elemental EDS maps. Bottom: diffraction patterns summed in the regions marked in the virtual dark-field image, exemplifying a guanine crystal and an amorphous iridophore. (c) Cryo-EELS spectra of the nitrogen K-edge collected from a guanine crystal showing the ratio between π^* pre-peaks that depend on the microenvironment's protonation potential.

observed in various organisms, including fish, reptiles, amphibians, cephalopods, and certain spiders. The application of cryo-STEM techniques allows us to correlate morphological features with crystallographic and analytical data, as they integrate real-space information with site-specific diffraction for each point traversed by the beam raster. Spatially resolved composition, mapped with EDS, and bonding information obtained through electron energy loss spectroscopy (EELS) further complement this correlative and site-specific analysis. In the case of the iridophores, the accumulation of nitrogen in electron-dense organelles may indicate an increase in guanine levels. Additionally, the observed change in the intensity ratio of the π^* pre-peaks to the nitrogen K absorption in high-resolution EELS (HREELS), obtained with a monochromated electron source of 50 meV energy spread, could suggest gradual neutralization in the acidic microenvironment of the vesicle during organelle maturation and crystal formation, as seen in X-ray absorption near edge structure (XANES).²⁶

It has been noted that 4D-STEM offers flexible control over electron fluence and significantly enhances the signal-to-noise ratio (SNR). This capability allows the collection of local diffraction information from beam-sensitive and weakly scattering materials.²⁷ However, a comprehensive examination of the limitations imposed by a low dose in studies focused on diffraction information has yet to be conducted.

In this study, we investigate the dose limitations concerning the detection limit of a diffracting volume embedded within a matrix. Specifically, we analyze the model case of a thin guanine crystal in an aqueous medium preserved in a cryo-EM sample. We first provide an estimate for the resolvable thickness of the crystalline slab with a basic analytical approach. We then verify and detail these considerations through more precise numerical calculations of the dynamical diffraction, inelastic scattering, and electron-counting detection, ensuring an appropriate understanding of the low-dose constraints.

Analytical formalism for the low-dose detection limit for Bragg reflections

The dose-limited detectable size of a diffracting crystal embedded within an isotropic scattering matrix, such as vitrified ice in a cryo-specimen, is determined by the statistics of electron collection. We consider the case of a thin crystalline platelet of thickness τ within a matrix of thickness t . The SNR can be expressed as

$$\frac{N_{hkl}}{\sqrt{N_{hkl} + N_{bg}}} \geq \kappa \quad (1)$$

assuming Poissonian counting statistics. Here, the signal counts are formed by the fraction of quasi-elastically scattered electrons N_{hkl} contributing to a Bragg peak (hkl) with a reciprocal lattice vector g_{hkl} contrasting with the background. The background counts N_{bg} are formed by electrons scattered in the matrix into the solid-angle segment surrounding g_{hkl} . The inequality relationship indicates that the SNR must exceed a certain threshold κ , which typically ranges between 2 and 5.

Electron scattering has to be treated as dynamical diffraction in general.²⁸ Due to diffraction from the periodical arrangements of atoms in crystalline materials, the intensity of the transmitted electron beam and any diffracted beam oscillates with depth with a periodicity that is known as the extinction distance.²⁸ We focus on the case of thin organic crystals with a thickness below the extinction distance for the reflection under consideration. We also assume a vanishing excitation error, *i.e.*, no deviation of the diffraction condition from the perfect Laue condition, to cover the case of a strong reflection. The excitation amplitude of the (hkl) reflection is then given by

$$N_{hkl} \approx N_0 \text{DQE} \alpha_{hkl} \tau^\varepsilon \quad \text{with} \quad \alpha_{hkl} = \frac{\lambda^2}{V_{uc}^2} \left| \frac{m}{m_0} F_{hkl} \right|^2 \quad (2)$$

where N_0 is the number of incident electrons in the beam profile, λ is the electron wavelength, F_{hkl} the structure amplitude for the crystal reflection (hkl), m and m_0 are the relativistic electron mass and rest mass, V_{uc} is the unit cell volume of the crystal, and ε is an exponent that is 1 for kinematical scattering and that takes the value 2 for dynamical scattering when a Bragg condition is closely fulfilled. The counting statistics are further affected by the detective quantum efficiency (DQE) of the sensor, which limits the fraction of the incident electrons contributing to utilized data.

The attenuation of the unscattered beam for a slab of crystalline material located at a depth t_0 within a matrix necessitates a correction to the number of incident electrons N_0 . Any diffracted beam propagating down from thickness t_0 to



the exit plane of the sample at thickness t can be considered as a primary beam that will experience multiple scattering as well. Therefore, for thick samples, the primary beam intensity will be subject to a cumulative attenuation represented by an exponential factor according to a Lambert–Beer law,²⁹ so that

$$N_{hkl} = N_0 \text{DQE} \alpha_{hkl} e^{-\mu_{\text{at}} t} \quad (3)$$

where μ_{at} is the attenuation factor and t the sample thickness. μ_{at} is determined primarily by the elastic scattering. For the case of a vitreous ice matrix, we extracted μ_{at} from the log–linear plot of the transmitted intensity *versus* the incident intensity from numerical multislice calculations presented below, which integrates up to a scattering angle of approximately 50 mrad. According to these numerical calculations, $\mu_{\text{at}} = 4.6 \times 10^{-5} \text{ \AA}^{-1}$, resulting in a loss on the order of 10% of electrons for an aperture of 50 mrad semi-angle.

For the matrix, we assume isotropic scattering; the intensity of the diffraction into diffuse scattering rings related to short-range order is obtained by averaging over all possible orientations of the short-range order motif, essentially accounting for all possible excitation errors. The integrated intensity adopts the kinematical form, according to Blackman;³⁰ at small thicknesses and larger scattering angle the scattered intensity is proportional the diffracting volume. For an amorphous matrix, we neglect short-range order to first approximation to derive a simplified expression since experimental data for ice scattering follows the approximation of the independent atom model well.³¹ Seifer³¹ found that the differential scattering cross-section for light elements with $Z > 4$ at larger scattering angles follows a power law $\propto \Theta^R$, $\Theta = \lambda g$. For elastic scattering to higher angles, the experimental value of $R = -3.7$ reproduces the tabulated NIST data well. The fraction of scattered electrons at large scattering angles is dominated by the elastic scattering, given by a simple proportionality:

$$N_{\text{bg}}^{\text{el}} \approx N_0 \text{DQE} \beta^{\text{el}} \Delta\Omega (t - \tau) \quad \text{with} \quad \beta^{\text{el}} = n_{\text{H}_2\text{O}} \frac{d\sigma_{\text{el}}}{d\Omega}(g) \quad (4)$$

where $\frac{d\sigma_{\text{el}}}{d\Omega}(g) \propto g^{-3.7}$ is the differential cross section for elastic scattering at a water molecule into the scattering angle λg , $\Delta\Omega$ is the solid angle of the detection element for integration, and $n_{\text{H}_2\text{O}} = 0.031 \text{ \AA}^{-3}$ is the number density of water molecules.

For light elements, inelastic scattering contributes substantially to the background counts. The inelastic collisions are localized and involve a loss of energy and change in wavelength. The effect on the diffraction focus is negligible, but the momentum transfer to larger angles involved results in a hazy background. A Lorentzian distribution of the angular scattering $1/(\Theta^2 + \Theta_E^2)$ was predicted, where Θ_E is half the ratio between the energy loss and collision energy.³² As has been recognized and shown in our previous results on quantitative scattering cross-section analysis *via* 4D STEM and EELS, the inelastic scattering in insulators occurs with an angular distribution much wider than the characteristic angle $\Theta_E \approx 0.1 \text{ mrad}$. The angular width of the plasmon scattering reflects the dielectric response of the matrix to the fast electron based on the momentum transfer to the longitudinal polarization wave emerging from the incoming electron. It is the large tail of the Lorentzian distribution associated with plasmon scattering that is often underestimated.³¹



Fig. 2 displays experimental data for the diffraction of vitrified ice with a thickness of 0.65 times the mean free path (mfp) for inelastic scattering, energy-filtered and non-filtered. Energy-filtered diffraction removes the background caused by the long tail of the momentum transfer in inelastic collisions. The effect is significant for an ice sample as the background at a typical lattice spacing of 1 nm is reduced by a factor of 10. At 10 1/nm, the background ratio between inelastic and elastic scattering *versus* elastic scattering is still about a factor of 2, which means that even for moderate ice thicknesses of one mean free path for inelastic scattering, the inelastic background affects the signal-to-noise ratio of all relevant Bragg reflections to 1 Å lattice resolution.

The inelastic scattering in ice at lower angles to a few mrad follows a single Lorentzian angular dependency $\propto \Theta^{-2}$ in ref. 31, hence

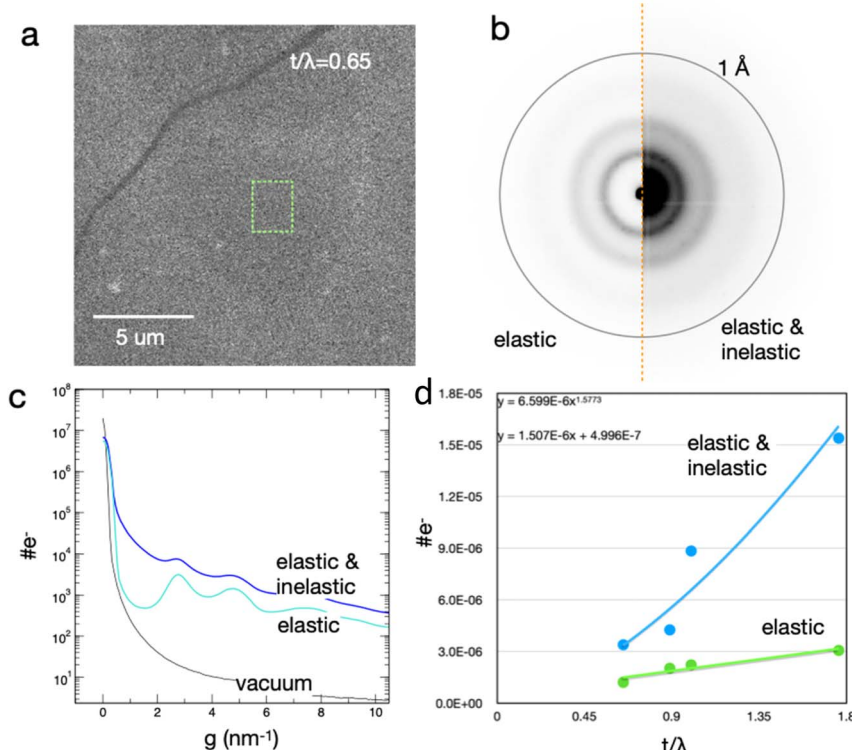


Fig. 2 Experimental scattering amplitudes of vitreous ice at various thicknesses for 200 keV electrons. (a) High-angle annular dark-field image of the sample prepared on holey carbon. The green area marks the region for a 4D STEM data recording in a hole of the carbon film. (b) Average of the nanobeam electron diffraction frames in the selected region. Left half: energy-filtered diffraction; right half: non-filtered, elastic and inelastic signal. The circle indicates 1 Å resolution at 25 mrad scattering angle. (c) Radial intensity profiles. (d) Plot of the elastic and total scattering amplitude for two sample positions, each position with two measurements at zero tilt and tilted to a 60 degree viewing angle to double the transmission depth. The plot shows the scattered intensity normalized to the number of incoming electrons at a scattering angle of 20 mrad. The mean free path for inelastic scattering is approximately 160 nm, measured from the projected view of channels drilled with the fine electron probe under normal incidence.



$$N_{\text{bg}}^{\text{in}} \approx N_0 \text{DQE} \beta^{\text{in}} \Delta Q (t - \tau) \text{ with } \beta^{\text{in}} = n_{\text{H}_2\text{O}} \frac{d\sigma_{\text{in}}}{dQ}(g) \propto g^{-2} \quad (5)$$

$\frac{d\sigma_{\text{in}}}{dQ}(g)$ is the differential cross section for water for inelastic scattering. The crossing point from inelastic dominant to elastic dominant scattering in water is around 10 mrad for 200 kV electrons.³¹ With eqn (3), (4), and (5), eqn (1) can be written as

$$\frac{\alpha N_0 \text{DQE} \tau^{\epsilon} e^{-\mu_{\text{at}}}}{\sqrt{N_0 (\beta^{\text{el}} + \beta^{\text{in}}) \Delta Q t \text{DQE}}} \geq \kappa \quad (6)$$

Eqn (6) has a solution for τ ; the asymptotic behavior for the case of a weak matrix and a strong matrix leads to:

$$\tau \geq \begin{cases} \left(\frac{\kappa^2}{\alpha_{hkl} N_0 \text{DQE}} \right)^{1/\epsilon} & (\beta^{\text{el}} + \beta^{\text{in}})(t - \tau) \ll \alpha_{hkl} \tau \quad \text{negligible matrix case} \\ \left(\frac{\kappa \sqrt{(\beta^{\text{el}} + \beta^{\text{in}}) \Delta Q t}}{\alpha_{hkl} \sqrt{N_0 \text{DQE}}} \right)^{1/\epsilon} & (\beta^{\text{el}} + \beta^{\text{in}})(t - \tau) \gg \alpha_{hkl} \tau \quad \text{strong matrix case} \end{cases} \quad (7)$$

The asymptotic case of the strong matrix deviates from the square-root dependence of the matrix thickness and number of incident electrons familiar from the Rose criterion,³³ which usually provides the appropriate formalism for the case of Gaussian counting statistics in the presence of a substantial background.³⁴ It shall be noted that for a crystal far from a zone-axis orientation, the solution will adopt the dependence in the Rose criterion, since the signal will adopt a linear dependence on τ .

For the example of an isolated β -guanine crystal in the $\langle 100 \rangle$ viewing direction, $|F_{hkl}|$ is 7.6 Å for $hkl = (060)$, α_{060} is roughly 1×10^{-7} Å⁻² at 200 kV and about 5000 primary electrons are required for detecting a 3 nm thick crystal free-standing over a vacuum with a signal-to-noise ratio of 2 on an ideal detector.

Experimental data for the scattering amplitude of the ice matrix was obtained from plunge-frozen samples using energy-filtered 4D-STEM. The thickness of the samples was independently measured using energy-loss spectra taken at the same location and by estimating the length of the projection of a hole prepared with a more intense electron probe at a tilted view. Elastic data was collected using an energy-selecting slit with a width of 15 eV, symmetrically centered around the zero-loss peak, which excluded both the bandgap transitions and plasmons equally. The data was recorded in electron-counting mode using a DECTRIS ELA detector within the linear response range. From Fig. 2, it is evident that there is a strong low-angle inelastic contribution signal below 10 mrad. Multiple inelastic scattering for the thickest sample leads to a deviation from linearity in the total signal, while the elastic part remains linear with thickness. The data suggests that energy-filtering provides a contrast gain over a significantly wide range of scattering angles for samples with a background contribution from materials with low atomic numbers. It is worth noting that the energy-filtered Bragg peak loses



contributions from inelastically scattered electrons at small-angle forward scattering. Therefore, the enhancement of the signal-to-noise ratio upon energy-filtering may not be as high as the reduction of the background between Bragg peaks may imply. Still, since the average Z number of an organic crystal is larger than that of the ice matrix, the overall effect will lead to an increase in contrast.

From the data in Fig. 2, we can derive a typical value for the parameter $\beta^{\text{el}} + \beta^{\text{in}}$ for the background scattering. For the thinnest samples, the independently measured thickness results in an inelastic mean free path of about 1600 Å. With a detection element of 3×10^{-8} sr, typical values for $\beta^{\text{el}} + \beta^{\text{in}}$ are around 1 per Å sr at 20 mrad.

Fig. 3 shows the estimate of τ for the case of a thick matrix, where the minimum detectable size increases to about 5 nm at comparable fluence of 5000 primary electrons for 100 nm thick vitreous ice. In the case of a 10 nm thick crystal embedded in a 200 nm thick matrix of vitreous ice, the same approximate primary number of 5000 electrons is required with a detector with an ideal DQE equal to 1.

The spatial resolution for imaging and orientation mapping depends on the maximum exposure available before noticeable radiation damage occurs. If D_c represents the maximum electron fluence that the specimen can tolerate before the diffraction data experiences unacceptable degradation, then a useful spatial resolution element—defined as a pixel with side length s and area s^2 —for 4D STEM mapping can be described as follows:

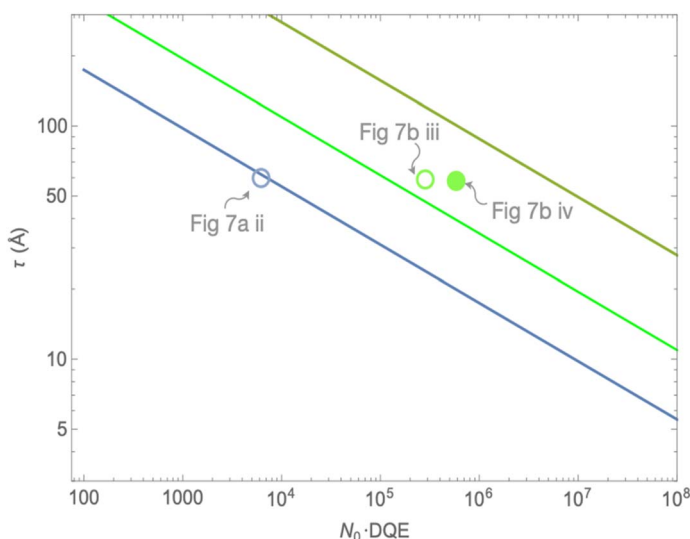


Fig. 3 Estimate of the detectable thickness τ of a guanine crystal in vitreous ice of thickness t according to eqn (7), for a primary electron energy of 200 kV as a function of the number of incident electrons N_0 and the DQE. The structure factor of the (060) reflection in guanine was used as the Bragg reflection for detection. The scattering amplitude of vitreous ice was derived from the experimental data shown in Fig. 2d. Three curves are plotted for $t = 1000$ Å (blue), $t = 2500$ Å (green), and $t = 5000$ Å (dark green). $V_{uc} = 579.2$ Å³ for β -guanine, $|F_{060}| = 7.6$ Å, $\alpha_{hkl} = 1 \times 10^{-7}$ Å², $\beta^{\text{el}} + \beta^{\text{in}} = 1$ Å⁻¹ sr⁻¹, $\mu_{\text{at}} = 4.6 \times 10^{-5}$ Å⁻¹, $\kappa = 3$, and $\Delta\Omega = 3 \times 10^{-8}$ sr. Circular markers represent numerical data presented later in the manuscript.



$$s = \sqrt{N_{\min}(\tau)/D_c} \quad (8)$$

Here, $N_{\min}(\tau)$ is the minimum number of incident electrons times the DQE to obtain a detection of the crystal of thickness τ . With a conservative D_c of 10 e^- per \AA^2 and requiring approximately 10^5 e^- to identify Bragg peaks, a limit of $s = 10 \text{ nm}$ is given for the spatial sampling with an electron beam non-overlapping between neighboring raster positions.

Numerical calculation of dynamical diffraction

Following the initial estimation of typical parameter ranges, we now proceed to a more refined numerical analysis based on a model that accurately represents a known ground truth. For a precise evaluation, it is crucial to dynamically treat the Bragg diffracted intensities, incorporating the effects of multiple scattering and inelastic scattering. Additionally, in the case of a thick matrix, angular beam spreading will cause the Bragg diffraction peak to broaden, whether due to the dispersion of the primary beam or the diffracted beam. The latter phenomenon will create an asymmetry in the detection threshold, depending on the crystal's position within the matrix. This effect was not considered in the initial analytical framework.

There are two prominent techniques commonly utilized for the numerical simulation of high-energy dynamical electron diffraction: the multislice method and Bethe's Bloch-wave method.³⁵ Both approaches involve solving the fundamental Schrödinger equation for high-energy electrons traversing through matter. For this discussion, the multislice method³⁶ has been selected due to its

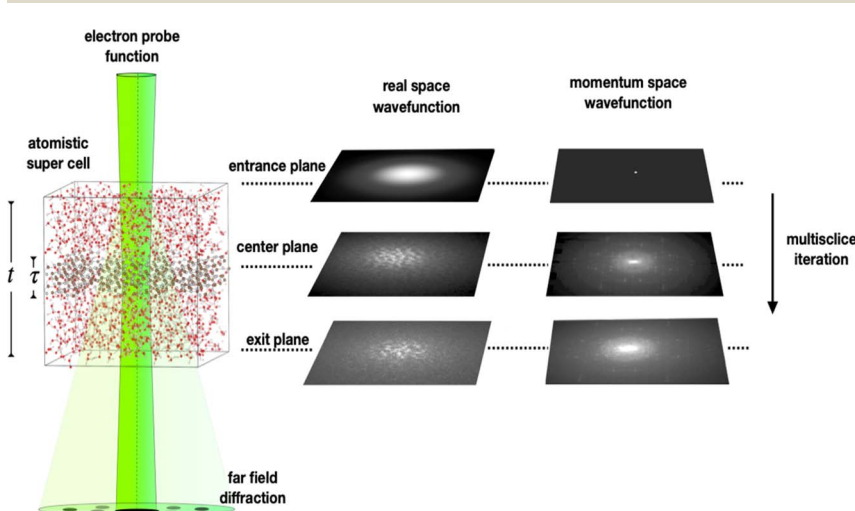


Fig. 4 Numerical simulation. A multislice iteration is used to calculate the diffraction of fast electrons in an atomic structure. The outcome is the complex-valued wave function at any plane within the atomic structure. The power of the wavefunction at the exit plane in real space and its Fourier spectrum, the diffraction pattern, are obtained. Here, the atomistic model consists of a slab of a β -guanine crystal with a thickness τ in the $\langle 100 \rangle$ viewing direction along the propagation direction, embedded in ice completing a total thickness t .



suitability for multi-component and arbitrarily coordinated atomistic supercells. In the multislice approach, the specimen is segmented into a series of thin slices along the thickness direction. The transmission and propagation of the electron beam are then calculated for each slice until reaching the specimen's exit surface.

The simulation of electron propagation was performed with Dr Probe.³⁷ Fig. 4 displays a schematic description of a multislice calculation to obtain simulated diffraction data. Inputs for the multislice iteration included a supercell composed of phase grating slices derived from a water model and crystalline guanine. Optimized atomic coordinates for amorphous vitrified ice were obtained through molecular dynamics simulations.³⁸ The multislice calculations considered the elastic scattering of electrons, applying the frozen lattice approximation for high-angle scattering. Atomic scattering factors were computed using the parameterization by Weickenmeier and Kohl.³⁹ Stochastic sets of random atomic displacements of thermal atom vibrations were generated for the frozen-state variants. Approximately 100 frozen lattice configurations were averaged for each simulation of a diffraction pattern in the detection plane. The scattering distribution was calculated for a diffraction-limited nanobeam electron probe with a semi-convergence angle of 0.4 mrad at an electron energy of 200 keV. The lateral field of view of $22\text{ nm} \times 22\text{ nm}$ was sampled with a 1024×1024 pixel grid, resulting in a Nyquist limit of 23.27 nm^{-1} and a simulation cutoff set at 15.5 nm^{-1} .

The effect of the inelastic scattering was included in the numerical simulation using a Monte Carlo approach. Inelastic scattering was incorporated using a heuristic plasmon scattering model, akin to the approach described in ref. 40. A random selection of electrons undergoes an inelastic scattering event according to an average inelastic scattering cross-section related to the mean free path, with a random scattering angle and energy losses following a probability distribution. The inelastically scattered electrons follow a path of elastic propagation until the next event or their exit from the lower sample surface. Therefore, the angular distribution of scattered electrons is built up by elastic and inelastic scattering during the multislice iteration.

For the numerical calculation of plasmon scattering in ice, we used a mean energy loss of 22 eV and a mean free path of 160 nm according to previous EELS measurements.³¹

In Fig. 5, the multislice simulation results for elastic *versus* elastic and inelastic diffraction are summarized. The case shows results for a 6 nm thick sample of β -guanine at the top, center, or bottom of an ice matrix with a thickness of 100 nm, 250 nm, or 500 nm, probed by electrons with 200 keV energy. We chose β -guanine in the $\langle 100 \rangle$ viewing direction for this example. In the experiment, a perfect zone-axis alignment of the crystal is a singular case. For this reason, beam precession was used to average over multiple excitation errors of the crystal's reciprocal lattice points to obtain a statistically more likely result. For precession, several hundred beam tilt sampling points were cumulated to obtain a complete diffraction data set.

Fig. 5 shows that for thicknesses t below the mean free path λ for inelastic scattering, $\lambda = 160\text{ nm}$, the differences in the signal-to-noise ratio of the diffraction peaks are subtle, becoming substantial when the sample thickness exceeds λ . For a thickness of 500 nm, the signal-to-noise ratio in the Bragg peaks drops below the detection threshold for the total scattering signal. Remarkably,



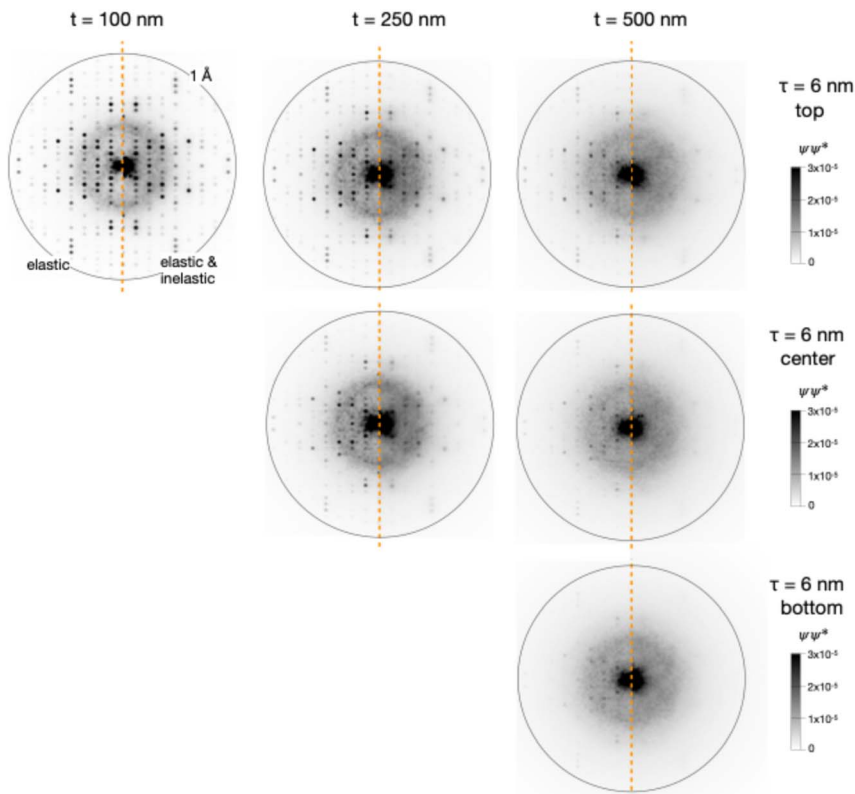


Fig. 5 Multislice calculation of nanobeam diffraction patterns of a 6 nm thick slab of β -guanine in an ice matrix with various thicknesses t . The simulation shows three cases of guanine at the top, *i.e.* at the entrance plane of the electron beam, the center and the bottom of the sample. The left part of each pattern shows the elastic contribution, and the right part shows the sum of elastic and inelastic contributions. The plots display the power of the electron wavefunction ψ , which is equivalent to the probability of electron detection. All maps are normalized to unity incident electron wave power and clipped to the same range from 0 to 3×10^{-5} .

the crystal will remain detectable in the elastic signal, a clear benefit of energy-filtered 4D STEM or diffraction tomography for cryo-EM of organic materials.

The simulation data reveals the effect on the contrast in the guanine diffraction peaks when the crystal is located further down from the beam entrance plane, related to the angular beam spreading, elastic and inelastic. This becomes obvious when comparing the top row simulation data in Fig. 5 with the bottom row for the sample thickness $t = 500$ nm. The highest contrast is obtained when the electron probe first interacts with the crystal before passing through the matrix. In contrast, placing the crystal at the exit plane results in lower contrast and detectability. Weak reflections become harder to detect. The resolution in the diffraction mode is limited by the angular broadening of the electron beam caused by multiple inelastic scattering inside the specimen. In the simulation, the semi-convergence angle of the incident beam of 0.4 mrad broadens to 1.1 mrad at the exit plane of a 500 nm thick slab of ice while developing extended Lorentzian



tails. This angular broadening reduces the signal-to-noise ratio of the diffraction peaks of specimens located at the bottom of a thick matrix layer and weaker reflections become difficult to detect.

The results in Fig. 5 are representations of the power of the electron wavefunction that emerges from the exit plane of the sample, normalized to the power of the wavefunction at the entrance plane. The latter is usually set to one, making the power spectra in Fig. 5 equivalent to probability maps for detecting an electron. With a large number of incident electrons, experiments will replicate these probability maps.

Low dose detection

We now focus on the scenario involving a finite number of incident electrons and the constraints imposed by exposure. Low-dose detection limits were calculated using an algorithm based on discrete binomial statistics, which we present here. In this algorithm, we derive the probability of detecting an electron in a specific position within the diffraction frame from the detection-plane wave function $\psi(g_x, g_y)$. Its power $p = \psi\psi^*$ represents the probability measure p to detect an electron in a detector array element (g_x, g_y) at any given time. We further establish that in the frame time δ , the electron source emits on average $\langle n(\delta) \rangle$ electrons with a corresponding statistical variance. At moderate extraction, the emission events can be regarded as uncorrelated, and the number $\langle n(\delta) \rangle$ reaching the sample and detection plane is the parameter in a Poisson distribution. Subsequently, a decision is made by identifying which elements of the detector array will register each electron, for each electron up to $\langle n(\delta) \rangle$. The decision is made using the probability measure p . Importantly, the pixel with the highest probability p is not necessarily the one that will detect the electron; rather, it simply has the highest likelihood of

Random process 1: $z = \text{Rand}(\text{PoissonPDF}(\gamma))$, $\gamma = \langle n(\delta) \rangle$

Random process 2: for each item in z , example for 10 detector pixels

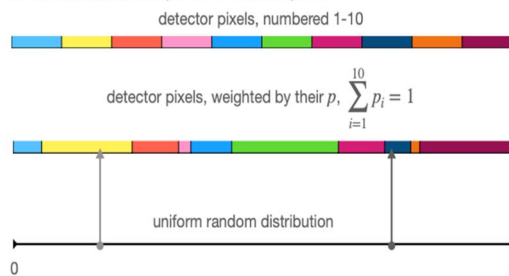


Fig. 6 Schematic for the calculation of low-dose images. Two random processes are involved. In process 1, the number of electrons detected in a single exposure frame during its exposure time is determined from a discrete Poisson distribution. A decision on which pixel will detect is made in random process 2, for each of the number of electrons determined in process 1. For computational reasons, a uniformly distributed random variable is mapped to an array with segments whose lengths are scaled according to the probability given by the power of the electron wavefunction at the exit plane of the sample in reciprocal space.



doing so. Computationally and to streamline the decision-making process, a uniform random distribution is mapped onto a linearized array of the detector pixel elements, with the length of each pixel element adjusted according to the probability measure p . Fig. 6 provides a brief overview of the two random processes involved in the calculation of low-dose images.

Fig. 7 presents the results for the model of β -guanine in ice. The panel compiles data for two ice thicknesses of 100 nm and 250 nm, considering the position of the guanine slab at either the top or the bottom of the sample, and the dependence on the number of electrons per diffraction frame. For clarity, a (033) reflection is marked. According to the single scattering approximation in eqn (6), the signal-to-noise ratio (SNR) for a reflection is proportional to a factor $\sqrt{N_0 \cdot \text{DQE}} / \sqrt{t}$. The numbers for this factor in nm^{-1/2} are given in red next to each figure. It is evident that this proportionality roughly holds for the thinner sample with a thickness of 100 nm. However, beyond the mean free path for inelastic scattering, we observe a deviation: the SNR for the (033) reflection of guanine at the top appears poorer for the $t = 250$ nm pattern with 2×10^5 incident electrons

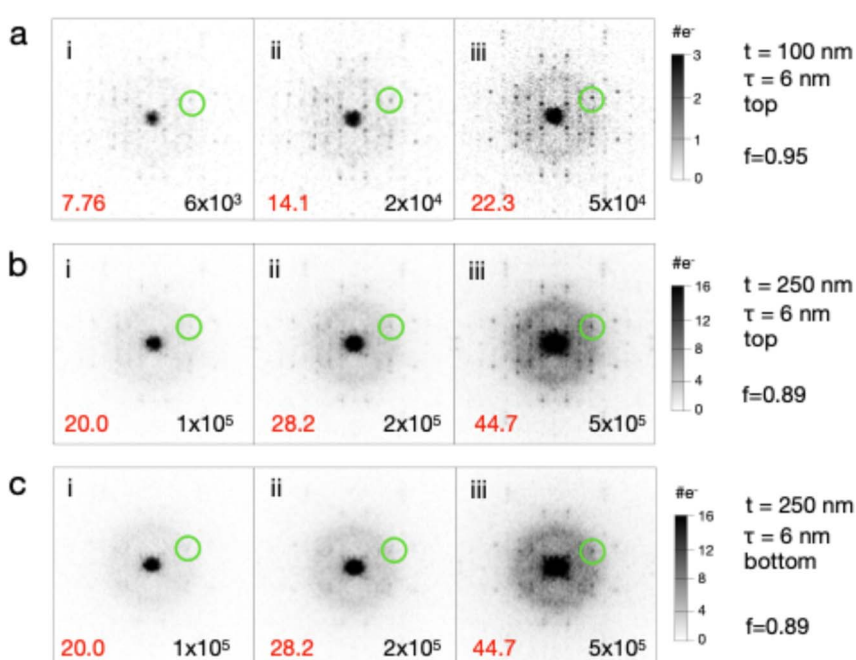


Fig. 7 Simulated low-dose electron nanobeam diffraction patterns for a model of β -guanine in an ice matrix. The figure displays two scenarios: guanine positioned at the top (a and b) and at the bottom (c) of the sample. t is the ice thickness and τ the thickness of the guanine crystal in the $\langle 100 \rangle$ viewing direction along the beam path. f is the fraction of electrons that remain at the exit plane of the sample, reflecting the 'absorption' related to high-angle scattering beyond the collection cut-off. From left to right, the quantity of incident electrons multiplied by the detector DQE increases (indicated by the black numbers). The red numbers represent the square root of the number of electrons divided by the square root of the thickness. A (033) reflection at a scattering angle of 9.85 mrad is highlighted as a guide for reference. The simulation parameters for the calculation of the electron wavefunction ψ match the parameters listed in the caption for Fig. 5.



than for the $t = 100$ nm pattern with 5×10^4 electrons. A rough validation of the SNR of the (033) reflection can be used to compare the simulation data with the analytical estimate in Fig. 3. These data points appear as circles in Fig. 3. The shift in the numerical data for Fig. 7b part ii and 7c part iii to higher fluence compared to the analytical estimate based on the single scattering approximation visually represents the deviation from the expected proportionality. This result suggests that, for moderate sample thicknesses of cryo-EM samples or cryo-EM lamellae obtained through focused ion beam milling with a thickness comparable to a single mean free path for inelastic scattering, it is crucial to consider the effects of multiple inelastic scattering and angular beam spreading.

Summary and conclusions

We developed an analytical description and procedures for numerically calculating the low-dose detection limits for thin crystals embedded in a thick matrix, particularly relevant for cryo-electron microscopy (cryo-EM) experiments. When samples exceed the mean free path for inelastic scattering, the detection limits worsen beyond the single scattering approximation. This is due to the broad angular spread of the inelastic scattering distribution and the beam broadening effect, resulting in a significant top-bottom effect on the detection limit. For samples that are 500 nm thick or more, energy-filtered detection is necessary to identify organic crystals smaller than 10 nm in thickness. As a general guideline, a fluence of a few thousand electrons should be recorded to clearly identify the Bragg peaks of organic crystals within a diffraction frame when the sample matrix is thinner than the mean free path for inelastic scattering. For thicker samples, the required fluence to detect the same peaks can increase by orders of magnitude.

For detection purposes, this indicates a limitation on the speed required for detector technology as well as on the achievable spatial resolution. The detection limits apply to any related technique that relies on diffraction contrast. In 4D STEM, this encompasses the contrasts observed in virtual diffraction contrast images, the identification of zone axis patterns, orientation mapping, and, by extension, diffraction tomography for phase identification. It is important to note that this discussion focuses on incoherent diffractive detection or imaging; coherent imaging will need to be addressed separately. For practical applications, the relevant factors for estimating the detection limits can be conveniently derived from multislice simulations as shown in this study. The formalism is applicable not only to organic crystals and their aqueous embedding for 4D STEM methods, but is also beneficial for the theoretical treatment of electron diffraction tomography and for various research fields, including pharmaceutical and polymer sciences.

Methods

Scanning transmission electron microscopy (STEM) images and 4D-STEM data were acquired in a double aberration-corrected Themis-Z microscope (Thermo Fisher Scientific Electron Microscopy Solutions, Hillsboro, USA (TFS)) at an accelerating voltage of 200 kV. STEM images were recorded with a Fischione Model 3000 detector. EDS data was acquired on a Super-X solid-state detector.



Cryo-samples were loaded into a Gatan 914 cryo-transfer holder. Zero-loss filtered 4D-STEM datasets were obtained with a CEOS CEFID (CEOS GmbH, Heidelberg, Germany) energy filter equipped with a DECTRIS ELA (DECTRIS AG, Baden, Switzerland) hybrid-pixel array detector. An electron probe with a convergence angle of 0.2 mrad and a real space probe diameter of several 10 nm was rastered across the sample for nanobeam diffraction experiments. The magnification was chosen to avoid beam overlap for neighboring sampling points. A primary beam current between 1 and 4 pA, a typical frame size of approximately $3 \times 3 \mu\text{m}^2$ and a frame time of 10 ms per raster position resulted in a total fluence of less than 2.0 e⁻ per Å². The 4D-STEM datasets were analyzed with the CEOS PantaRhei Software and custom-written software.

For the multislice calculation of the diffraction data we used Dr Probe.³⁷ Phase gratings with a size of 22 nm × 22 nm with 1024 × 1024 samples were generated from atomistic supercell data for guanine and water. The water supercell was optimised by molecular dynamics (MD) refinement according to ref. 38. The Nyquist limit for the calculations was 23.27 nm⁻¹, with a simulation cut-off of 15.5 nm⁻¹. An electron energy of 200 kV and a probe-semi-convergence angle of 0.4 mrad were assumed for the electron probe. The probe was diffraction-limited with zero lens aberrations. Frozen lattice simulations were carried out with 100 configurations, with a precession tilt up to 0.3 mrad in 9 tilt settings. The inelastic plasmon scattering parameters were a maximum of two inelastic events per incoming electron, *i.e.*, per frozen lattice configuration. A mean free path for inelastic scattering of 160 nm with a characteristic inelastic scattering angle of 0.1 mrad and a critical angle of 2 mrad were used.

Data availability

The supercell data for the multislice calculations for water and guanine has been deposited at <http://zenodo.org>, DOI: <https://doi.org/10.5281/zenodo.14749851>.

Conflicts of interest

There are no conflicts to declare.

Acknowledgements

We thank the Irving and Cherna Moskowitz Center for Nano and Bio-Nano Imaging at the Weizmann Institute of Science for the support of the electron microscopy studies.

References

- 1 G. Falini, *et al.*, Control of aragonite or calcite polymorphism by mollusk shell macromolecules, *Science*, 1996, **271**, 67–69.
- 2 F. C. Meldrum, Calcium carbonate in biomineralisation and biomimetic chemistry, *Int. Mater. Rev.*, 2003, **48**, 187–224.
- 3 F. Nudelman and N. Sommerdijk, Biomineralization as an Inspiration for Materials Chemistry, *Angew. Chem., Int. Ed.*, 2012, **51**, 6582–6596.



4 J. W. C. Dunlop, *et al.*, Artful interfaces within biological materials, *Mater. Today*, 2011, **14**(3), 70–78.

5 D. Gur, *et al.*, *Adv. Funct. Mater.*, 2017, **27**, 1603514.

6 B. A. Palmer, *et al.*, The organic crystalline materials of vision: structure–function considerations from the nanometer to the millimeter scale, *Adv. Mater.*, 2018, **30**, 1800006.

7 L. Addadi, L. Kronik, L. Leiserowitz, D. Oron and S. Weiner, Organic Crystals and Optical Functions in Biology: Knowns and Unknowns, *Adv. Mater.*, 2024, **36**, 2408060.

8 J. D. Rimer, *et al.*, Crystal growth inhibitors for the prevention of L-cystine kidney stones through molecular design, *Science*, 2010, **330**, 337–341.

9 K. N. Olafson, G. P, *et al.*, Mechanisms of hematin crystallization and inhibition by the antimalarial drug chloroquine, *Proc. Natl. Acad. Sci. U. S. A.*, 2015, **112**, 4946–4951.

10 I. Weissbuch and L. Leiserowitz, Interplay between malaria, crystalline hemozoin formation, and antimalarial drug action and design, *Chem. Rev.*, 2008, **108**, 4899–4914.

11 E. C. Theil, Ferritin: The Protein Nanocage and Iron Biomimetic in Health and in Disease Elizabeth, *Inorg. Chem.*, 2013, **52**, 12223–12233.

12 S. Yao, B. Jin, Z. Liu, C. Shao, R. Zhao, X. Wang and R. Tang, *Adv. Mater.*, 2017, **29**, 1605903.

13 A. Engel, Biological applications of the scanning transmission electron microscope, *J. Struct. Biol.*, 2022, **214**, 107843.

14 S. G. Wolf, *et al.*, Cryo-scanning transmission electron tomography of vitrified cells, *Nat. Methods*, 2014, **11**, 423–428.

15 P. Rez, *et al.*, Exploring the theoretical basis and limitations of cryo-STEM tomography for thick biological specimens, *J. Struct. Biol.*, 2016, **196**, 466–478.

16 A. Engel and C. Colliex, Application of scanning transmission electron microscopy to the study of biological structure, *Curr. Opin. Biotechnol.*, 1993, **4**, 403–411.

17 O. L. Krivanek, *et al.*, Atom-by-atom structural and chemical analysis by annular dark-field electron microscopy, *Nature*, 2010, **464**, 571–574.

18 O. L. Krivanek, *et al.*, Vibrational spectroscopy in the electron microscope, *Nature*, 2014, **514**, 209–212.

19 D. A. Muller, Atomic-Scale Chemical Imaging of Composition and Bonding by Aberration-Corrected Microscopy, *Science*, 2008, **319**, 1073–1076.

20 J. S. Wu, *et al.*, Imaging and elemental mapping of biological specimens with a dual-EDS dedicated scanning transmission electron microscope, *Ultramicroscopy*, 2013, **128**, 24–31.

21 I. Lazić, *et al.*, Single-particle cryo-EM structures from iDPC-STEM at near-atomic resolution, *Nat. Methods*, 2022, **19**, 1126–1136.

22 C. Ophus, Four-Dimensional Scanning Transmission Electron Microscopy (4D-STEM): From Scanning Nanodiffraction to Ptychography and Beyond, *Microsc. Microanal.*, 2019, **25**, 563–582.

23 K. A. Spoth, *et al.*, Dose-Efficient Cryo-STEM Imaging of Whole Cells Using the Electron Microscope Pixel Array Detector, *Microsc. Microanal.*, 2017, **23**, 804–805.

24 L. Zhou, *et. al.*, Low-dose phase retrieval of biological specimens using cryo-electron ptychograph, *Nat. Commun.*, 2020, **11**, 2773.



25 S. Seifer, *et al.*, Optimizing Contrast in Automated 4D STEM Cryotomography, *Microsc. Microanal.*, 2024, **30**, 476–488.

26 Z. Eyal *et al.*, Controlled pH Alteration Enables Guanine Accumulation and Drives Crystallization within Iridosomes, *bioRxiv*, 2024, preprint, DOI: [10.1101/2024.07.20.604036](https://doi.org/10.1101/2024.07.20.604036).

27 J. Donohue, *et al.*, Cryogenic 4D-STEManalysis of an amorphous-crystalline polymer blend: Combined nanocrystalline and amorphous phase mapping, *iScience*, 2022, **25**, 103882.

28 L. Reimer and H. Kohl, Transmission Electron Microscopy, *Springer Series in Optical Sciences*, Springer, 2008.

29 M. Hayashida and M. Malac, High-Energy Electron Scattering in Thick Samples Evaluated by Bright-Field Transmission Electron Microscopy, Energy-Filtering Transmission Electron Microscopy, and Electron Tomography, *Microsc. Microanal.*, 2022, **28**, 659–671.

30 M. Blackman, On the Intensities of Electron Diffraction Rings, *Proc. R. Soc. London, Ser. A*, 1939, **173**, 68–82.

31 S. Seifer, *et al.*, Quantitative atomic cross section analysis by 4D-STEM and EELS, *Ultramicroscopy*, 2024, **259**, 113936.

32 C. Colliex, and C. Mory, Quantitative aspects of scanning transmission electron microscopy, in *Quantitative Electron Microscopy*, ed. J. N. Chapman and A. J. Craven, SUSSP Publications, Edinburgh, 1984, pp. 149–216.

33 A. Rose, A Unified Approach to the Performance of Photographic Film, Television Pickup Tubes, and the Human Eye, *J. Soc. Motion Pict. Eng.*, 1946, **47**, 273–294.

34 A. E. Burgess, The Rose model, revisited, *J. Opt. Soc. Am. A*, 1999, **16**, 633–646.

35 H. Bethe, Theorie der Beugung von Elektronen an Kristallen, *Ann. Phys.*, 1928, **392**, 55–129.

36 J. M. Cowley and A. F. Moodie, The Scattering of Electrons by Atoms and Crystals. I. A New Theoretical Approach, *Acta Crystallogr., Sect. A*, 1957, **10**, 609–619.

37 J. Barthel, Dr Probe: A software for high-resolution STEM image simulation, *Ultramicroscopy*, 2018, **193**, 1–11.

38 N. Elad, *et al.*, Detection of isolated protein-bound metal ions by single-particle cryo-STEM, *Proc. Natl. Acad. Sci. U. S. A.*, 2017, **114**, 11139–11144.

39 A. Weickenmeier and H. Kohl, Computation of the atomic inner-shell excitation cross-sections for fast electrons in crystals, *Philos. Mag. B*, 1989, **60**, 467–479.

40 B. G. Mendis, An inelastic multislice simulation method incorporating plasmon energy, *Ultramicroscopy*, 2019, **206**, 112816.

